Computational and experimental analysis of droplet transportation/jetting behaviours driven by thin film surface acoustic waves

Mehdi H. Biroun[a], M.T. Rahmati[b], M. Jangi[c], Ran Tao[d], B.X. Chen[e], Y. Q. Fu[f,*]

[a]: Faculty of Engineering and Environment, Northumbria University, Newcastle upon Tyne NE1 8ST, UK; Email: Mehdi.Hosseini@Northumbria.ac.uk.

[b]: Faculty of Engineering and Environment, Northumbria University, Newcastle upon Tyne NE1 8ST, UK; Email: Mohammad.Rahmati@Northumbria.ac.uk.

[c]: Department of Mechanical Engineering, University of Birmingham, Birmingham, B15 2TT, UK; Email: M.Jangi@bham.ac.uk.

[d]: Faculty of Engineering and Environment, Northumbria University, Newcastle upon Tyne NE1 8ST, UK; Email: R.Tao@Northumbria.ac.uk.

[e]: Institute of Mechanical, Process & Energy Engineering, School of Engineering & Physical Sciences, Heriot Watt University, Edinburgh, Scotland, EH14 4AS, UK. Email: B.Chen@HW.ac.uk.

[f]: Faculty of Engineering and Environment, Northumbria University, Newcastle upon Tyne NE1 8ST, UK; Email: Richard.Fu@Northumbria.ac.uk.

*Corresponding author: Prof. Richard Yongqing Fu

Room E409, Ellison Building, Northumbria University,

Newcastle upon Tyne, NE1 8ST, UK

T: +44 (0)191 2274662

M: +44(0)7939839127

Richard.Fu@Northumbria.ac.uk

Abstract

A Coupled Level Set Volume of Fluid (CLSVOF) approach has been applied to investigate severe deformation/transportation/jetting behaviours of sessile droplet driven by thin-film surface acoustic waves (SAW) devices. For validation of this computational method, a series of experimental studies of droplet transportation/jetting were performed using ZnO/Si thin film based SAW devices with resonant frequencies ranging from 64.49 MHz to 271.36 MHz. Good agreements between the computational and experimental results showed the capability of the developed CLSVOF method in modelling complex acoustofluidics phenomena such as significant internal streaming, pumping and jetting of the droplet driven by the propagating SAW.

Results obtained from the computational model are used to clarify the fluidic mechanisms of droplet oscillation and wobbling behaviours during transportation. Numerical results reveal the liquid streaming patterns and airflow velocity field around the droplet at different stages of transportation/jetting process. Effects of droplet volume, the resonant frequency of SAW devices and applied SAW power on droplet transportation/jetting were investigated both theoretically and experimentally. In particular, comparisons between experimental and computational results showed that the model predicted well the minimum RF power to start droplet pumping and jetting at various resonant frequencies.

Keywords: Surface Acoustic Wave, Droplet, Micro Actuator, Transportation, Jetting, CLSVOF

1. Introduction

Surface Acoustic Wave (SAW)[1] based microfluidics has become an intensive research area due to the growing demands for liquid element control within the microsystems [1–7]. SAW-based acoustofluidic devices can be used for different bio-sampling functions, such as mixing, heating, pumping, jetting, separation and atomization of fluids with volumes in the scale of microliters, and their applications include biochemical analysis, disease diagnosis, DNA sequencing, DNA hybridization, drug screening, and drug delivery systems [8,9]. Applying a radio frequency (RF) signal to a set of interdigital transducers (IDT) made on a piezoelectric material can generate surface acoustic waves (SAWs). Constructive interference occurs while the frequency of the RF signal, ω, is set equal to v_s/λ (where v_s is the sound velocity of substrate ate and λ is the distance between two fingers of IDT, and thus SAWs are generated and travel on the surface of the piezoelectric material [10,11].

SAW can manipulate a sessile droplet located on a piezoelectric substrate within its propagation path through fluid-SAW interactions [12]. The differences between sound velocities in the fluid domain and piezoelectric substrate lead to dissipation of SAW energy into the fluid medium. Depending on SAW amplitude and frequency as well as properties of piezoelectric substrate material, a pressure field or body force is generated inside the droplet along the Rayleigh angle (θ_R).

$$\theta_R = \sin^{-1}\frac{v_L}{v_S} \tag{1}$$

where v_L is wave velocity in liquid [13]. A schematic view of SAW propagation in both mediums is illustrated in Fig. **1**(a).

[1]

Nomenclature

Latin Symbols

Symbol	Description	Unit
A	Wave amplitude	m
a	Coefficient of interface normal vector calculation	
b	Coefficient of interface normal vector calculation	
$\boldsymbol{Ca}$	Capillary number	
$\boldsymbol{F_{SAW}}$	SAW force	kg·m·s^{-2}
$\boldsymbol{f_\sigma}$	Surface tension	kg·m·s^{-2}
$\boldsymbol{g}$	Gravitational acceleration vector	m.s^{-2}
H	Smoothed Heaviside function	
k	SAW wave number	m^{-1}
n	Normal vector	
P	RF power	kg·m^2·s^{-3}
$\boldsymbol{p}$	Pressure	pa
S	Sign function of initial LS function	
t	Time	s
$\boldsymbol{u}$	Velocity	m.s^{-1}
v	Sound velocity	m.s^{-1}
x, z	Coordination directions	

Subscripts Symbols

Symbol	Description
adv	Advancing
cl	Contact line
d	Dynamic
e	Static
f	Interface
g	Gas
l	Liquid
rec	Receding
s	Solid
w	Wall

Greek Symbols

Symbol	Description	Unit
α	Volume fraction of liquid	
α_1	Attenuation coefficient	
Γ	Constant	
Δx	Mesh size	
$\delta(\phi)$	Dirac function	
ϵ	Interface thickness	m
θ	Dynamic contact angle	
θ_R	Rayleigh angle	
κ	Curvature of the interface	
λ	Distance between two fingers of IDT	m
μ	Fluid viscosity	m^2.s
ρ	Density	Kg.m^{-3}
σ	Surface tension coefficient	N.m^{-2}
τ	Artificial time	s
$\boldsymbol{\tau_k}$	Viscous stress tensor	pa
ϕ	LS function	
ω	Wave frequency	MHz

Abbreviations

Symbol	Description
CFD	Computational Fluid Dynamics
CLSVOF	Coupled Level Set Volume of Fluid
IDT	Interdigital Transducer
LS	Level Set
RF	Radio Frequency
SAW	Surface Acoustic Wave
VOF	Volume of Fluid
ZnO/Si	Zinc Oxide – Silicon

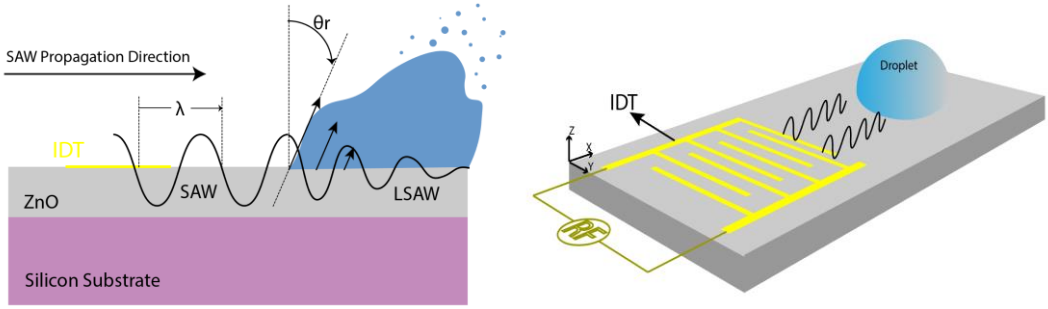

(a) (b)

Fig. 1. (a) 2D Schematic illustration of SAW propagation along a ZnO/Si SAW device substrate, (b) 3D illustrations of SAW device and wave propagation

Recently, droplet streaming[4,6,14–17], transportation (sometimes called pumping) [18–23] and jetting [24–28] phenomena have been extensively investigated, and the droplet transportation and jetting have been realised on different substrates [19,21,29–31]. There is a rapid development of numerical methods and computational resources in the last couple of decades, and several numerical studies of droplet behaviour driven by SAW have been carried out alongside the experimental works. For example, Sankaranarayanan et al. [10] used a coupled-field fluid-structure interaction (FSI) model to simulate the acoustic streaming. They predicted the internal streaming velocity of the droplet to vary from 1 μm/s to 1 cm/s. Alghane et al. developed a 3D model to analyse the internal streaming behaviour of the sessile droplet subjected to SAW. Ai and Marrone [32] studied the droplet coalescence by a focused SAW in a 2D space. Rezk et al. [33] reported the simulation studies of steady poloidal flow in sessile droplet induced by focused SAW, which were in an excellent agreement with experimental results. Darmawan and Byun [25] conducted a quasi-quantitative analysis of acoustic radiation pressure distribution within a droplet and demonstrated that the jetting of the droplet is exposed by a localised and focus pressure distribution. Riaud et al. [34] developed a cost-effective computational method to study the effect of the viscosity on the acoustic streaming of the droplets driven by SAW. Although the numerical studies of SAW-based microfluidics have been performed for decades, there is still a lack of numerical models which can simulate severe deformation of sessile droplets, or capture the droplet interface deformation, or predict the precise internal liquid flowing during the droplet transportation and jetting induced by SAW. A fundamental and theoretical understanding of the droplet transportation and jetting and its internal flowing driven by SAWs is critical for successful designs and development of innovative types of lab-on-a-chip, acoustofluidics and bio-detection systems.

Despite the seemingly simple process of droplet pumping or transportation, it includes severe droplet interface deformation and movement; the intricate two-phase flow patterns occur at the microscale, and complex streaming behaviours. Therefore, it is challenging to study the multiphysics problem of transportation and jetting process through the experiments systematically. The objective of the present study is to develop a computational method to capture the large deformation, fast transportation, and jetting of the droplet and its interfaces by SAW to obtain a detailed theoretical clarification of droplet actuation processes.

2. Numerical Method

2.1. Governing Equations

For computational modelling of the droplet, the multiphysics nature of the acoustofluidic problem needs to be considered. This includes two-phase flow and interfacial phenomena such as surface tension, dynamic contact angles and liquid-interactions with acoustic waves. Assuming that heat transfer and evaporation are negligible, the isothermal two-fluid (liquid droplet and air) system of SAWs acting on the droplet can be described by conservations of mass and momentum,

$$\frac{\partial}{\partial t}(\rho) + \nabla.\boldsymbol{u} = 0 \tag{2}$$

$$\frac{\partial}{\partial t}(\rho\boldsymbol{u}) + \nabla.(\rho\boldsymbol{u}\boldsymbol{u}) = -\nabla p + \nabla.\boldsymbol{\tau_k} + \rho\boldsymbol{g} + \boldsymbol{f_\sigma} + \boldsymbol{F_{SAW}} \tag{3}$$

where u is velocity, g the gravitational acceleration vector, p the pressure, and ρ the density. The viscous stress tensor is defined by $\boldsymbol{\tau_k} = \mu(\nabla\boldsymbol{u} + \nabla\boldsymbol{u^T})$. The system is driven and balanced by the forces of SAW action, $\boldsymbol{F_{SAW}}$, the fluid viscosity, μ , and the surface and interfacial tensions, $\boldsymbol{f_\sigma}$. The forces due to the surface tension and fluid properties of density and dynamic viscosity will be discussed in the next sub-section. Here to consider

the energy transferred by SAW to the fluid medium, we use the approach proposed by Shiokawa et al. to define the SAW action force[13],

$$\boldsymbol{F_{SAW}} = -\rho(1+{\alpha_1}^2)^{\frac{3}{2}}A^2\omega^2 k exp(2[kx+\alpha_1 kz]) \quad (4)$$

where$\alpha_1 = -\boldsymbol{j}\left(\sqrt{1-(v_s/v_l)^2}\right)$ is attenuation coefficient, A the wave amplitude, ω the wave frequency and k the SAW wave number, which can be calculated by a linear function of the wave frequency [10]. To simulate the 3D pattern of energy transferred by SAW to the fluid medium, F_{SAW} is assigned to be at its maximum value at TPCL on each row of CFD mesh along the propagation direction, and since k is a negative number, it will decay exponentially along x and z directions.

2.2. Interfacial streaming, flowing and deformation

Among all the methods developed for modelling interfacial flows, the volume of fluid (VOF) and the level-set methods are two Eulerian based methods which have been widely used. While the VOF method conserves the mass, its accuracy in capturing sharp interface and curvature calculations is low in surface tension dominant problems [35]. On the other hand, the LS method can accurately calculate the curvature, and also the captured interface by this method is smooth and sharp [36]. However, mass conservation is frequently violated by the LS method. In this study, we use the CLSVOF approach proposed by Sussman and Pucket to obtain a sharp interface and conserve the mass across the interface [37].

In the VOF method, the VOF function, α, is defined as the liquid volume fraction of the cell. Thus the value of α is between zero and one in the interface region and zero and one for air and liquid. The transportation of the interface can be described by,

$$\frac{\partial \alpha}{\partial t} + \nabla.(\boldsymbol{u}\alpha) = 0 \quad (5)$$

Accordingly, the physical properties of the two fluids, e.g., the density and viscosity of the liquid (l) and gas (g), can then be defined as,

$$\rho = \rho_l \alpha + \rho_g(1-\alpha) \quad (6)$$

$$\mu = \mu_l \alpha + \mu_g(1-\alpha) \quad (7)$$

The volumetric surface tension force, f_σ, can be calculated from:

$$\boldsymbol{f_\sigma} = \sigma\kappa(\alpha)\nabla\alpha \quad (8)$$

where σ is the surface tension coefficient of the liquid in the gas, and $\kappa(\alpha)$ is the curvature of the interface. The curvature is the magnitude of the normal interface flux at each cell, and it indicates the direction of this flux.

$$\kappa(\alpha) = -\nabla.\frac{\nabla\alpha}{|\nabla\alpha|} \quad (9)$$

As α is defined as a discontinue step function of the gradient of α at the interface, accurate calculation of the curvature at the interface is difficult.

A level-set field, ϕ, is defined where the interface is located at $\phi = 0$. The initialised function ϕ_0 is a sign function which is positive in the liquid phase and negative in the gas phase. ϕ_0 is derived by solving the re-initialisation equation:

$$\frac{\partial \phi}{\partial \tau} = S(\phi_0)(1-|\nabla\phi|) \quad (10)$$

where $S(\phi_0)$ is the sign function of initial LS function and τ the artificial time. The solution of the re-initialisation equation is converged to a signed distance function when $|\nabla\phi|$=1. The interface based on ϕ is much smoother and sharper compared to that based on the volume fraction α. Subsequently, the curvature at the interface and the surface tension force can be determined equation (11) and (12).

$$\kappa(\phi) = -\nabla.\frac{\nabla\phi}{|\nabla\phi|} \quad (11)$$

The LS model works well, in comparison with the VOF method, in terms of keeping the interface sharp and accurate with a reasonable numerical cost. By using the Dirac function $\delta(\phi)$, the surface tension force, f_σ, is confined to a narrow region around the two-phase interface.

$$f_\sigma = \sigma\kappa(\phi)\delta(\phi)\nabla\phi \tag{12}$$

$$\delta(\phi) = \begin{cases} 0 & |\phi| > \epsilon \\ \frac{1}{1.5\Delta x}\left(1 + \cos\left(\frac{\pi\phi}{0.75\Delta x}\right)\right) & |\phi| \leq \epsilon \end{cases} \tag{13}$$

where Δx is the mesh size.

2.3. Dynamic Contact Angle Modeling

The dynamic contact angle is used to express the adhesion of the fluid to the solid surface. Using experimental observation, the long list of factors affecting the dynamic contact angle can be shortened to the three-phase contact line (TPCL) velocity, fluid physical properties and surface treatment method [38]. To locally correct the interface normal vector field on the wall boundary, $\vec{n}_{f,0}$ which is obtained from the re-construction of the interface algorithm, we use the procedure introduced by Familie [39]. In our work, the dynamic contact angle model proposed by Cox is implemented to predict the contact angle of the droplet with the solid surface [40].

$$\theta_d{}^3 = \theta_e{}^3 + 144Ca \tag{14}$$

$$Ca = \frac{\mu_{li} u_{cl}}{\sigma} \tag{15}$$

To calculate the dynamic contact angle, the magnitude of TPCL velocity, u_{cl} and its direction must be estimated. In this study, we follow Afkhami's approach to calculate the TPCL velocity and direction [41]. The governing equations were solved using OpenFOAM-4.x.

3. Experimental Details

In this study, we choose ZnO/Si SAW devices, as the conventional bulk material based SAW devices are brittle and cannot be easily integrated with electronics for control and signal processing. It is desirable to develop SAW devices based on piezoelectric thin-film materials such as ZnO and AlN, which could be seamlessly integrated into a single lab-on-chip (LOC) device at a low cost, with full integration functions and good reliability at high SAW powers [42,43]. ZnO films with a thickness of 3.5 μm were deposited on (100) silicon wafers using a direct current magnetron sputter system (NS3750, Nordiko). The vacuum was maintained at ~0.65 Pa during the deposition with an Ar/O_2 flow ratio of 1/3. The Cr/Au IDTs with the thickness of 20/100 nm were fabricated onto the ZnO/Si substrate using a standard photolithography and lift-off process. The bi-directional IDTs consist of 30 pairs of fingers, with an aperture of 5 mm. In this study, to compare the experimental results of droplet transportation at different SAW frequencies, IDTs with different spatial periodicities were used, e.g., 64, 32, 20 and 16 microns. The SAW devices were then coated with CYTOP (Asahi Glass Co.) hydrophobic layers. An HP8752A RF network analyser was used to measure the resonant frequency and the amplitude of the SAW devices. The Rayleigh wave was generated using an RF signal generator (Marconi 2024, Plainview, USA), and then amplified by a power amplifier (Amplifier research, 75A250, Souderton, USA). The measured resonant frequencies of the fabricated ZnO/Si SAW devices and calculated velocities are listed in Table 1. Water droplets of different sizes (from 1 to 8 microliters) were placed in front of the IDTs using a micropipette. The droplet internal streaming, severe deformation, transportation and jetting behaviour were recorded using a high-speed video camera (Photron XLR Express).

Table 1. Measured frequencies and calculated velocities of ZnO/Si SAW devices

Wavelength (μm)	Frequency (MHz)	Sound Velocity on the device ($m.s^{-1}$)
64	64.49	4127.36
36	116.96	4210.56
20	210.48	4209.60
16	271.32	4341.12

4. Results and discussion

The computational domain for all the cases in this section is a rectangular box. Initially a spherical droplet of radius R_0 and contact angle of θ_0 is positioned on the left end of the bottom wall. The velocity field is initialized as u = 0. Two-step local mesh refinement is employed to refine the mesh in the droplet moving area. Mesh refinements are along the Z direction. The dimensions of the computational domain and the mesh refinement strategy are selected after a series of test simulations for droplet moving area.

-The Navier Slip boundary condition is implemented according to Afkhami et al. [41] to relax the no-slip boundary for the velocity at the bottom patch. Details of the input parameters, fluid properties, solution method and boundary conditions are summarized in Table 2.

Table 2. Input parameters and modelling setup for numerical simulation.

Input parameters	Value	
Static contact angle	110°	
Wave number[10]	-1813 m^{-1}	
Attenuation coefficient	2.598	
Surface tension coefficient	0.0707106 $Kg.s^{-2}$	
Properties	Water	Air
Density	999.13 $Kg.m^{-3}$	1.1839 $Kg.m^{-3}$
Kinematic viscosity	8.917×10^{-7} $m^2.s$	15.52×10^{-6} $m^2.s$
Solution methods	Setup	
Computational domain	rectangular box	
Mesh refinement	Two-step local mesh refinement in the Z direction	
Time steps	Variable time step with maximum Courant number of 0.3	
Field	Boundary condition	
Velocity	Bottom Plane	Navier Slip
	Side and top plane	pressureInletOutletVelocity
Pressure	Bottom Plane	fixedFluxPressure
	Side and top plane	fixedFluxPressure
LS and VOF field	Bottom Plane	Dynamic contact angle
	Side and top plane	Zero gradient

To perform a convergence test for grid resolution, simulation results of droplet transportation on two different computational domains with a dimension of $4 \times 1.6 \times 2.2$ (mm) and minimum mesh sizes of Δx=0.025 mm and Δx=0.0125 mm are compared with experimental data. Simulation has been performed for a water droplet transportation at 25℃ with a volume of 1 µL on a SAW device with the resonant frequency of 64.46 MHz. All the calculations are performed in parallel on 6 Dual Intel Xeon E5-2680 v4 14 core 2.4GHz CPUs (336 cores). The difference between the two captured liquid-gas interfaces is negligible. The average droplet velocities obtained are compared to the experimental results as listed in Table 3. It is seen from Table 3 that the droplet transportation velocity for both domains has insignificant differences. Consequently, all the computations are done in a domain with a droplet radius to a minimum cell size ratio of ~30 to optimise the computational costs.

Table 3. A comparison between the droplet transportation velocities for two different grid resolution strategies

Minimum Cell size (mm)	Droplet radius to cell size ratio $(R_0/\Delta x)$	Total number of the cells	Calculation time (hours)	Droplet average velocity (m.s^{-1})	The difference from Experimental results
0.025	28.24	901,120	~11	0.1418	-2.74%
0.0125	56.48	7,208,960	~66	0.1412	-3.15%

4.1. Model validation with experimental results

To validate the CLSVOF solver and contact angle model, the experimental data are compared with the simulation results in this section. XZ middle plane of the CFD mesh domain, droplet's initial condition, and

important boundary conditions are illustrated in Fig. 2(a). The initial location of the droplet, SAW direction, and mesh structure is presented in Fig. 2(b). The computational domain is a rectangular box with a dimension of $8.0 \times 2.8 \times 4.0$ (mm) Consisting of 3,476,480 hexahedral cells. Simulation has been performed for a droplet of water with a volume of 5 µl and initial radius of 1.17 mm. The SAW with the frequency of 64.49MHz is applied to the liquid medium from the left side. Calculations are performed in parallel for ~35 hours.

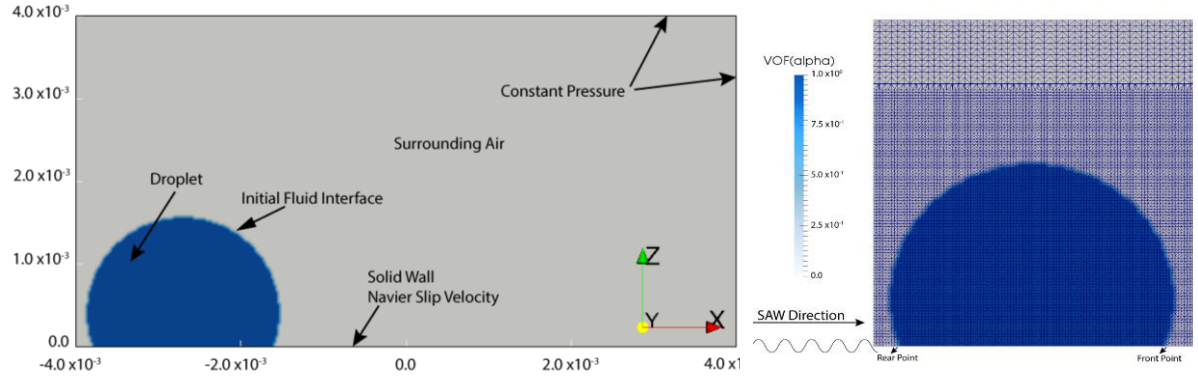

(a) (b)

Fig. 2. Numerical setup (a) An isentropic view of simulation geometry with the initial position of the droplet. The wave direction in all the simulations is from left to right, (b) A cross-section view of initial droplet condition and mesh refinement strategy. Rear point is defined as the point closer to the SAW device IDTs and vice versa.

A qualitative comparison between computational and experimental results of droplet transportation on a ZnO/Si SAW device is presented in

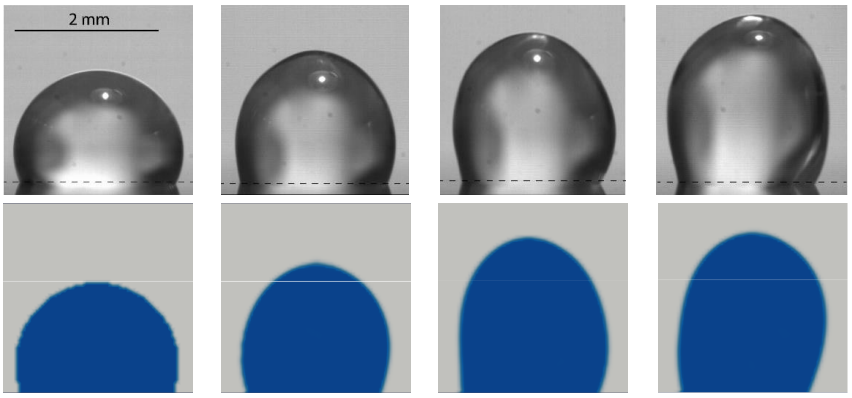

Time = 0 ms 12 ms 25 ms 37 ms

Fig. 3. A comparison between experimental and simulation results of droplet shape variation.

Based on the simulation model, a comparison between the velocity of the front and rear points of the droplet is presented in Fig. **4**. The reasonably good agreement between the experimental and simulation results confirms that the numerical model can be used to simulate the droplet actuation by SAW. Since the TPCL motion is highly dependent on the dynamic contact angle model, the comparison between experimental and simulation results also validate the implementation of dynamic contact angle boundary condition.

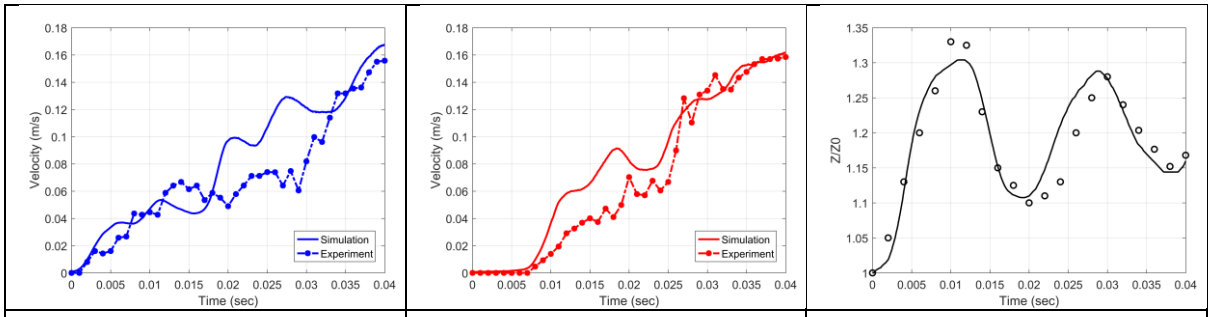

(a) (b) (d)

Fig. 4. A comparison between experimental and simulation results for droplet transportation velocity, (a) rear point (b) front point. (c) Droplet tip position while pumping;

4.2. Mechanisms of Droplet transportation

As the precision of the CLSVOF method and contact angle model is confirmed, the mechanism of droplet's severe deformation and transportation are now investigated in this section using CFD results of the same case. The SAW force is at its maximum value at the rear point and decay exponentially along x and z-direction. There are three key parameters in droplet behaviour during its pumping, e.g., the SAW force which generates momentum inside the fluid, the viscous force which dissipates the energy transferred by SAW into the fluid medium, and the surface tension force which diverts the direction for the momentum at the interface.

Before applying the SAW force, the TPCL is a circle. By applying the force for ~4.3 msec, the rear side of the TPCL shrinks toward the centre of the circle while the front side is motionless. The initial droplet deformation changes the contact angle. Meanwhile, the curvature at the droplet interface increases slightly. From equation (8), we know that surface tension is proportional to the curvature of the droplet interface. Thus, the surface tension at the interface of the deformed droplet increases. During this time, the applied SAW force overcomes the inertial liquid inertia. After 4.3 msec, due to the increase of momentum inside the droplet, the front side of the TPCL starts to move.

Consequently, the droplet advancing contact angle is increased, its tip is raised, and the contact area between the solid and liquid is decreased. After 12 msec, when the ratio of droplet tip height to its initial value (Z/Z_0) is equal to ~1.3, the droplet tip starts to descent. The velocities of the rear and front points are also decreased due to the following two reasons. Firstly, the curvature of the surface and surface tension are increased, which cancels the increase of the vertical momentum of the SAW force. Secondly, the lower contact area between the solid and the liquid leads to a reduced SAW energy transfer from the solid surface to the liquid medium. As soon as the ratio of Z/Z_0 reaches to ~1.1, SAW energy transferred is large enough to push droplet tip upward again. Droplet tip oscillation is presented in Fig. 4 (c).

Using our simulation model, we can predict both the streaming patterns of the surrounding air and the internal droplet, which have never been reported in the literature before. The total velocity of each cell centre in the liquid medium during the droplet transportation can be described as the sum of two velocities; e.g., streaming velocity and linear velocity of droplet parallel to the solid surface. To explain the air and liquid streaming patterns during first 6 msec, the time history of ϕ on droplet's middle plane overlaid by total velocity vectors is illustrated in Fig. 5. In the initial 29 msec of droplet pumping, the slopes of droplet velocity in two sides of the TPCL are not similar. This different velocity slopes from both sides create a wobbling movement of the droplet at the first 29 msec of the droplet pumping. After this time, the velocities of two sides of the droplet tend to have the same trend and the wobbling of the droplet starts to disappear.

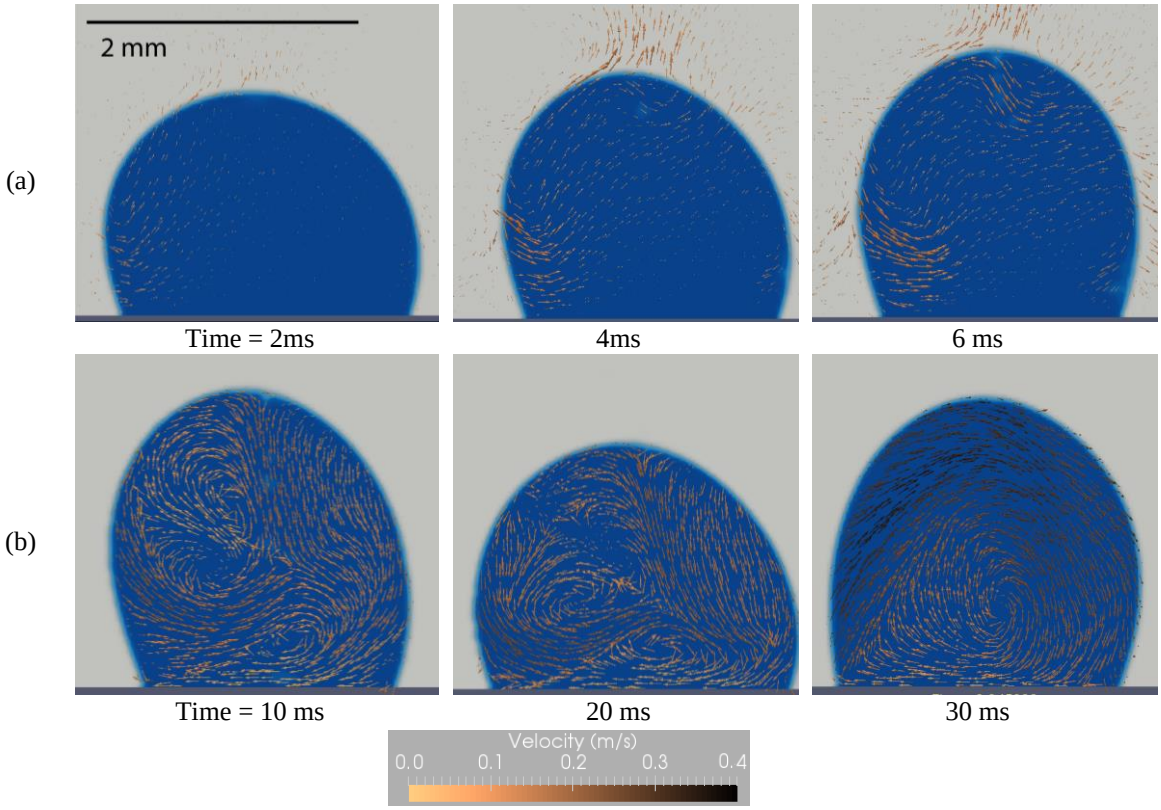

Fig. 5. (a) Snapshots of droplet central vertical section overlaid by velocity vectors during the start of the droplet pump. Their magnitude scales velocity vectors, (b) Internal streaming development while pumping, streaming velocity vectors are coloured by velocity vector magnitude.

To show the internal streaming pattern inside the droplet, the linear velocity of the droplet is subtracted from the x component of velocity vectors. Temporal evolutions of all the vectors inside the fluid medium are shown in Fig. **5**(b). Initially, the droplet is wobbling, and two annular vortexes can be observed inside the droplet. The lower vortex creates a rolling movement of the droplet while the higher vortex creates a twin annular flow, which is the main reason for droplet tip wobbling. The higher vortex disappears after 26 msec and the centre of the lower vortex moves toward the front point.

As time evolves and after 30 msec, a fully developed vortex can be observed inside the droplet which corresponds to the rolling movement of the droplet on the solid surface. The 3D streamlines of internal streaming inside the droplet after 32 msec are presented in The 3D streamlines of internal streaming inside the droplet after 32 msec are presented in Fig. 6 (a-b). The corresponding magnitudes of velocity vectors at the same time are shown in Fig. 6 (c). The airflow velocities near the interface are quite high. According to these results, due to the density difference between gas and liquid phase, the air velocities near the droplet have a negligible influence on the droplet interface shape.

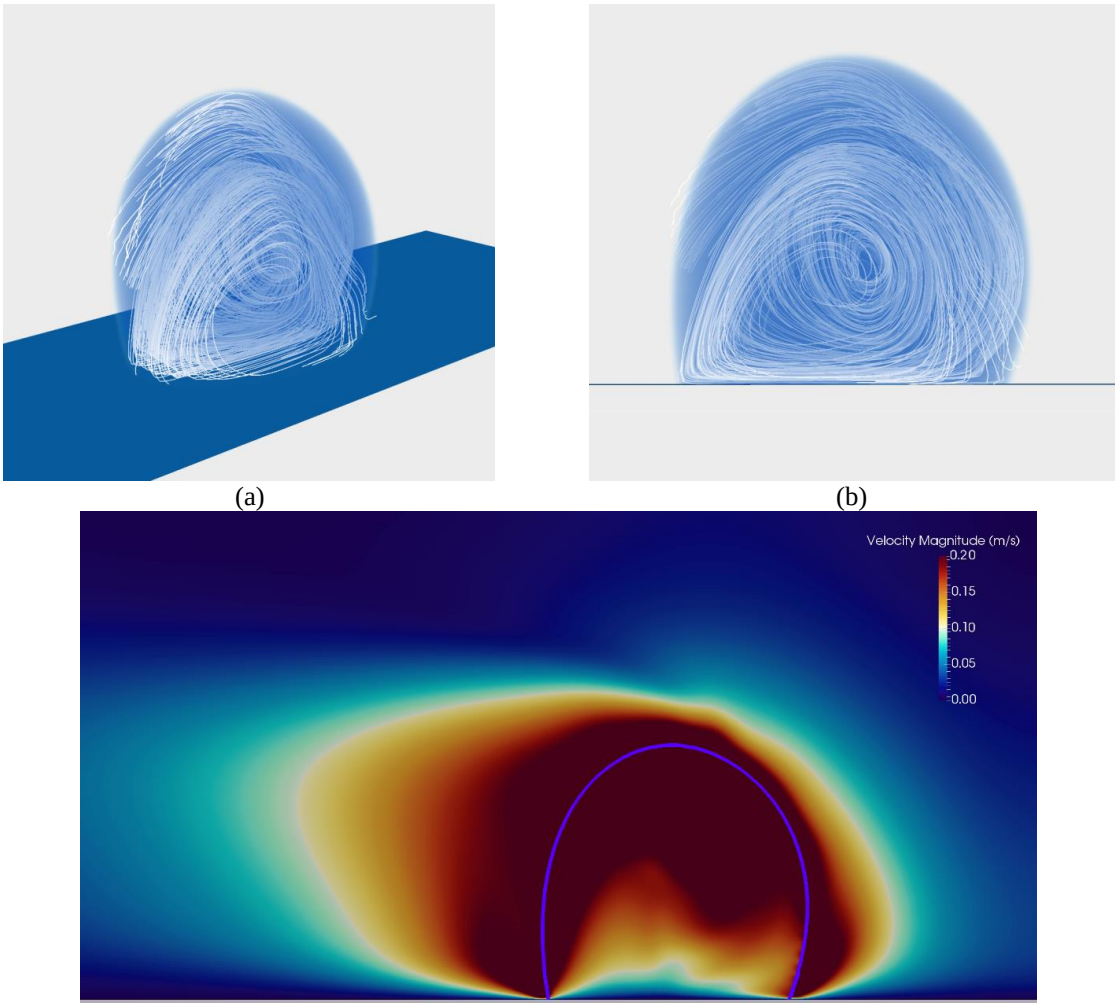

Fig. 6. Numerical 3D illustrations of complex internal streaming pattern inside the droplet after 32 msec after applying SAW (a) Tilted view, (b) Cross-section view perpendicular to SAW direction, (c) Velocity field for droplet and surrounding air of the droplet after 32 msec of calculation.

4.3. Key Influencing Parameters for droplet transportation

We have identified three key SAW parameters for further studies, as we need to use our newly proposed model to predict some new phenomena which can be derived from these simulation results.

4.3.1. SAW power

To investigate the effect of the SAW power on transportation behaviour of the droplet on the piezoelectric substrate, four cases were simulated. For all the cases, the wave frequency was kept constant at 64.50 MHz. The water droplet has a volume of 5 µl with an initial contact angle of 110°. To change the wave powers for different cases, four different wave amplitudes of 150, 250, 350, 420 (Å) were applied in equation (4) and the CFD calculation was performed up to 45 msec. Fig. **7** illustrates the velocity results of the droplet and the ratio of droplet tip height to initial height at the different steps of the simulation.

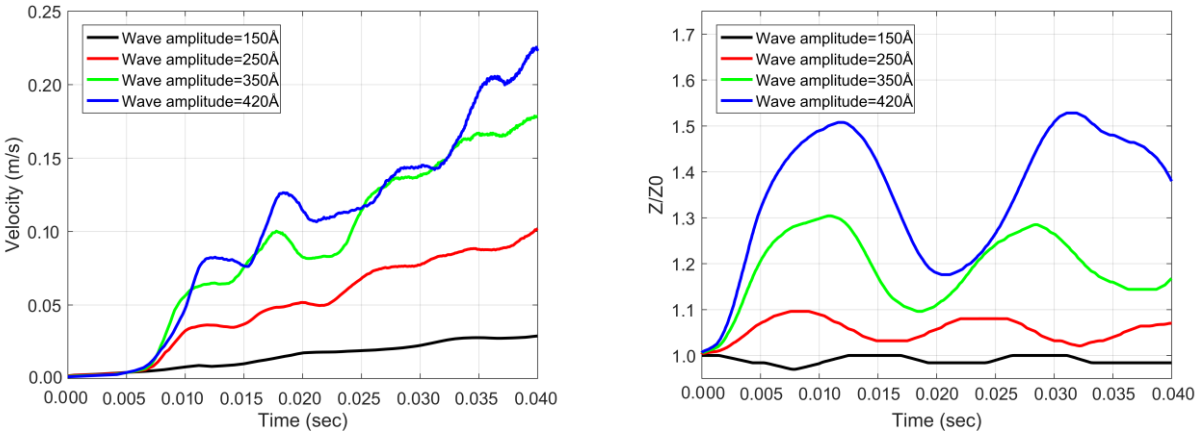

(a) (b)

Fig. 7. Simulation results for droplet transportation with different wave power, (a) droplet front point velocity, (b) droplet tip height

Experimental observations have shown that at each frequency, by increasing the SAW power, different microfluidic functions such as internal streaming, transportation and jetting can be obtained [19]. At each frequency, transportation occurs at a certain range of SAW amplitude, which is increased by increasing the resonant frequency of the device [44]. At SAW amplitudes between 30 to 200 Å, the amount of energy transferred from the solid surface to the fluid medium is low, and surface tension and viscous force are large enough to keep the droplet in its initial spherical droplet. Whereas, with further increasing the SAW amplitude, The SAW vertical momentum is high enough to reach the droplet surface and thus the droplet is deformed.

4.3.2. Droplet volume

In this section, the effect of droplet volume on transportation behaviour of the droplet is investigated. For all the cases, the SAW frequency is fixed at 64.49 MHz, and the initial contact angle is 110°. During the simulation, the ratio of the amount of SAW force to droplet volume constant is kept a constant, and the ratio of SAW amplitude to droplet diameter is also kept a constant. More details about the simulation details for this section is presented in Table 4.

To compare the droplet deformation, the obtained ratios of droplet tip height to its initial value, Z/Z_0, are presented in Fig. 8. An interesting observation for the cases with droplet volumes of 1 and 2 µl is the effect of droplet diameter on interface deformation. At this situation, surface tension is high enough to resist the vertical momentum created by SAW force and avoid the significant deformation of the droplet.

Table 4 simulation parameters to compare the effect of droplet volume in pumping

Droplet Volume (µl)	Wave Amplitude (A)	Droplet Diameter(mm)	CFD mesh size	Number of CFD mesh cells	Calculation time (hours)
1	204.61	0.684	$6.0 \times 1.6 \times 1.6(mm)$	~1.0 million cells	~12
2	257.86	0.862	$6.0 \times 2.0 \times 2.0(mm)$	~1.5 million cells	~14
5	350	1.17	$8.0 \times 2.8 \times 2.6(mm)$	~3.7 million cells	~35
8	408.92	1.367	$12.0 \times 3.1 \times 3.0(mm)$	~5.0 million cells	~52

With the increase of the droplet volumes, the oscillation of droplet is more significant due to lower curvature at the droplet interface and thus lower surface tension. Part of the SAW energy is used to deform the

droplet, and the droplet velocity is decreased when the droplet has a larger volume. The frequency of the droplet oscillation is also found to be inversely proportional to its volume.

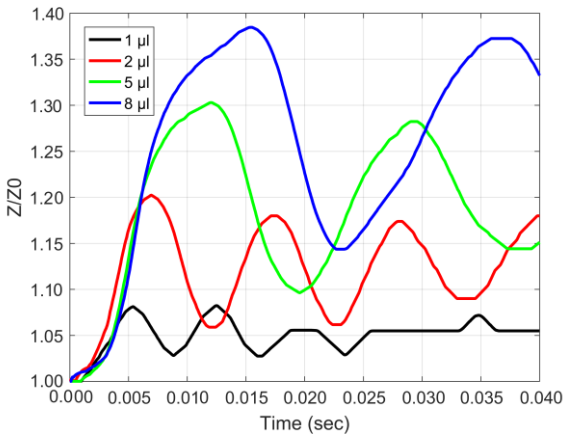

Fig. 8. The ratio of droplet tip height to initial value during transportation with different droplet volume.

4.3.3. SAW resonant frequency

To study the effect of resonant frequency on droplet actuation by ZnO/Si SAW device, in this section, we present the simulation results in two parts.

Firstly, four different cases with different device resonant frequencies of 64.49, 116.96, 210.48 and 271.32 MHz were defined. The wave amplitude and initial contact angle are kept constants at 350Å and 110° respectively. At higher frequencies, the actuation area by the SAW force is limited to the rear edge. However, the magnitude of the force in this area is much larger. A comparison between experimental and computational results for droplet transportation velocities at different SAW frequencies are shown in Fig. **9**(a). The droplet front point velocity is decreased with the increase of the resonant frequency as the attenuation length of SAW decrease by increasing the frequency, and less energy is dispatched inside the fluid medium at a constant wave power.

Secondly, to link the experimental and computational results, a set of simulations were performed to find the minimum wave amplitude to start droplet transportation or jetting. Experimental results show that by increasing the resonant frequency of the SAW device, the attenuation length is decreased, and thus, much less energy is dispatched from the surface to the fluid medium [19]. As the wavenumber is a linear function of frequency, by increasing the frequency, the wavenumber is increased, and the SAW force is attenuated in a shorter length among x and z directions. However, the magnitude of the force in the SAW agitated area is much larger. The total SAW force dissipated into the fluid medium and its dissipation distance are significantly reduced by increasing the frequency.

To compare the simulation and experimental results of droplet transportation by SAW waves at different frequencies, it is vital to define a mathematical relationship between RF power applied to the SAW device and SAW amplitude. Here, we follow an empirical correlation between experimental and simulation results to identify the normalized SAW amplitude, A/λ, by the RF power. The experimental results used here to fit the data are minimum RF power to start droplet transportation and jetting at different wavelengths with a ZnO/Si SAW device:

$$\frac{A}{\lambda} = 6.72 \times 10^{-6} P^{1.94} + 1.52 \times 10^{-6} P^{0.91} \qquad (16)$$

where P is the applied RF signal power in Watts. Fig. **9**(b) shows the simulated minimum SAW amplitude normalized by wavelength to start droplet transportation and jetting at different frequencies. The comparison between the experimental and simulation results shows that the computational model can predict droplet behaviour. Mixing area is defined as an area in which the applied power creates internal streaming while the droplet is stationary.

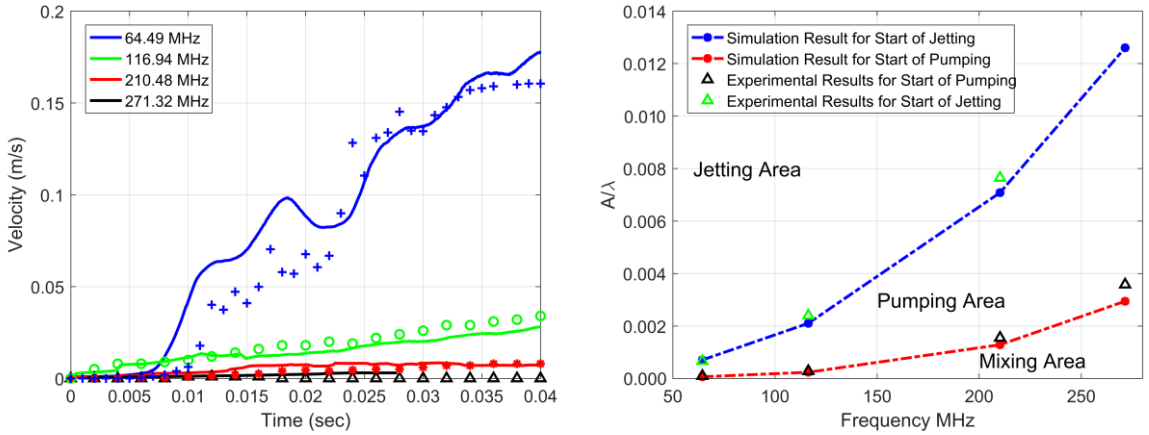

(a) (b)

Fig. 9. (a) Droplet front point velocity at different resonant frequencies; (b) A comparison between simulation and experimental results for minimum A/λ to start transportation and jetting

To design an optimum microfluidic SAW pump operated at a specific resonant frequency, the range of applied RF power to enhance internal streaming, transportation or jetting is critical. Due to the accuracy of the developed computational model, it can be used to predict the acoustofluidic behaviour at different RF power ranges. Comparing the minimum A/λ value to start jetting and transportation at different frequencies, the ratio between minimum power for jetting and transportation is decreased by increasing the frequency.

4.4. Droplet jetting behaviour

Droplet jetting can happen when the acoustic energy transferred from solid surface to the liquid phase is large enough to overcome the surface tension and gravitational force, and the droplet interface deforms until the droplet is separated from the surface along the Rayleigh angle [45]. To show that the newly developed code is capable of simulating droplet jetting, we reproduce the jetting phenomena for a droplet of 5 µl on a SAW device with the resonant frequency of 271.32 MHz. The measured static contact angle for a sessile droplet on this device is 114°. Wavenumber and attenuation coefficient for this sample set at 425 and 2.47 consequently [46]. A comparison between experimental and simulation results is presented in Fig. 10. The results clearly show that the developed code can capture the droplet interface during the jetting. The simulation results are overlaid by the velocity field inside the middle droplet plane. Velocity vectors after 3 ms of simulation show that there is developing streaming, at the left corner of the droplet. Droplet deformation is also pushing the surrounding air and creating an airflow around the droplet tip. After 11 ms, there is a strong flow pattern inside the droplet, which pushes the droplet up and also an air vortex can be observed in the left side of the droplet. Interestingly after the droplet separation from the surface, the internal streaming velocity is lower because of viscous damping and two air vortexes are created under the droplet.

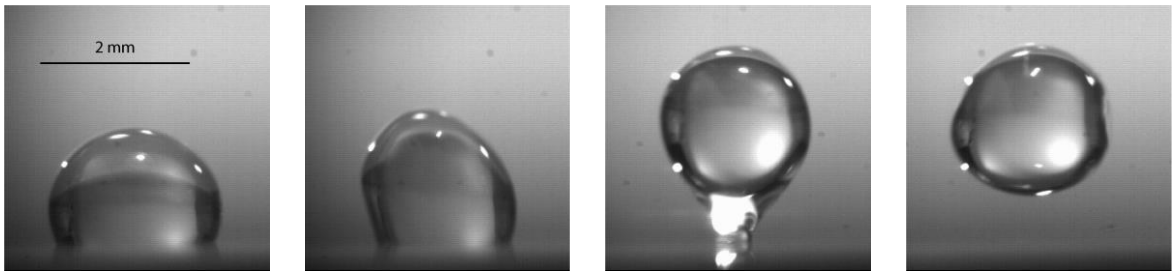

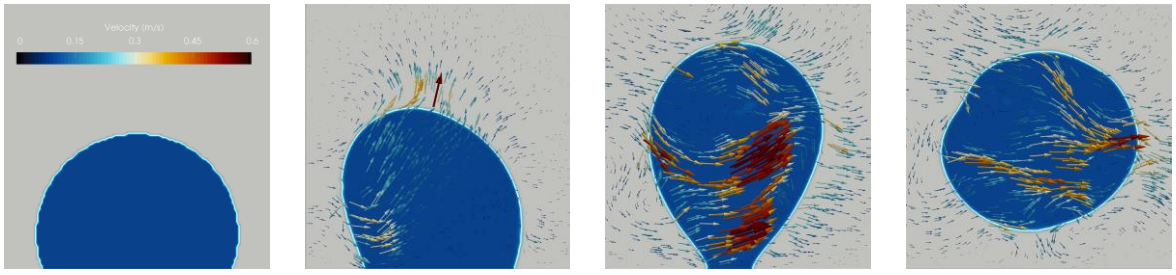

Time = 0 ms 3 ms 11 ms 16 ms

Fig. 10. A comparison between experimental and simulation results of droplet jetting by SAW device with a resonant frequency of 271.32 MHz. Scaled velocity vectors overlay simulation results.

5. Conclusions

In Summary, Droplet transportation and jetting on a solid piezoelectric surface of different SAW devices are analysed with a developed CLSVOF solver. Droplet translation by ZnO/Si Saw device is simulated, and A good qualitative agreement between the experimental and computational results is obtained. The results showed that the computational model could be used to predict the dynamic behaviour of droplet transportation by different SAW devices. The key factors affecting droplet translation is then numerically investigated.

Furthermore, it is observed that there is a critical wave amplitude at each frequency that droplet starts to move on or ejected from the solid surface. Moreover, an equation is proposed based on computational results to calculate the wave amplitude from the RF power of the SAW device to predict minimum power to start droplet transportation and jetting. Finally, droplet jetting by the SAW device is simulated, and the internal velocity field during the jetting process is revealed by the computational results.

Acknowledgement

The authors would like to acknowledge the financial support received from Engineering Physics and Science Research Council of UK (EPSRC EP/P018998/1 and EP/R010633/1).

6. References

[1] Wang K, Zhou W, Lin Z, Cai F, Li F, Wu J, et al. Sorting of tumour cells in a microfluidic device by multi-stage surface acoustic waves. Sensors Actuators, B Chem 2018;258:1174–83. doi:10.1016/j.snb.2017.12.013.

[2] Wiklund M, Green R, Ohlin M. Acoustofluidics 14: Applications of acoustic streaming in microfluidic devices. Lab Chip 2012;12:2438. doi:10.1039/c2lc40203c.

[3] Whitesides GM. The origins and the future of microfluidics. Nature 2006;442:368–73. doi:10.1038/nature05058.

[4] Wixforth A. Acoustically Driven Programmable Microfluidics for Biological and Chemical Applications. J Lab Autom 2006;11:399–405. doi:10.1016/j.jala.2006.08.001.

[5] Li S, Carlier J, Toubal M, Liu H, Campistron P, Callens D, et al. High frequency acoustic on-chip integration for particle characterization and manipulation in microfluidics. Appl Phys Lett 2017;111. doi:10.1063/1.5003414.

[6] Friend J, Yeo LY. Microscale acoustofluidics: Microfluidics driven via acoustics and ultrasonics. Rev Mod Phys 2011;83:647–704. doi:10.1103/RevModPhys.83.647.

[7] Collignon S, Friend J, Yeo L. Planar microfluidic drop splitting and merging. Lab Chip 2015;15:1942–51. doi:10.1039/C4LC01453G.

[8] Gedge M, Hill M. Acoustofluidics 17: Theory and applications of surface acoustic wave devices for particle manipulation. Lab Chip 2012;12:2998. doi:10.1039/c2lc40565b.

[9] Fukuoka D, Utsumi Y. Fabrication of the cyclical fluid channel using the surface acoustic wave actuator and continuous fluid pumping in the cyclical fluid channel. Microsyst Technol 2008;14:1395–8.

doi:10.1007/s00542-007-0548-1.

[10] Sankaranarayanan SKRS, Cular S, Bhethanabotla VR, Joseph B. Flow induced by acoustic streaming on surface-acoustic-wave devices and its application in biofouling removal: A computational study and comparisons to experiment. Phys Rev E - Stat Nonlinear, Soft Matter Phys 2008;77:1–19. doi:10.1103/PhysRevE.77.066308.

[11] Ralib AAM, Nordin AN, Alam AZ, Hashim U, Othman R. Piezoelectric thin films for double electrode CMOS MEMS surface acoustic wave (SAW) resonator. Microsyst Technol 2015;21:1931–40. doi:10.1007/s00542-014-2319-0.

[12] Wixforth A, Strobl C, Gauer C, Toegl A, Scriba J, Guttenberg Z V. Acoustic manipulation of small droplets. Anal Bioanal Chem 2004;379:982–91. doi:10.1007/s00216-004-2693-z.

[13] Showko Shiokawa, Yoshikazu Matsui TU. Study on SAW Streaming and its Application to Fluid Devices. Jpn J Appl Phys 1990;29:137–9. doi:https://doi.org/10.7567/JJAPS.29S1.137.

[14] Dentry MB, Yeo LY, Friend JR. Frequency effects on the scale and behavior of acoustic streaming. Phys Rev E - Stat Nonlinear, Soft Matter Phys 2014;89:1–11. doi:10.1103/PhysRevE.89.013203.

[15] Karlsen JT, Qiu W, Augustsson P, Bruus H. Acoustic streaming and its suppression in inhomogeneous fluids 2017:1–6. doi:10.1103/PhysRevLett.120.054501.

[16] KOSTER D. NUMERICAL SIMULATION OF ACOUSTIC STREAMING ON SURFACE ACOUSTIC WAVE-DRIVEN BIOCHIPS 2007;29:2352–80. doi:10.1137/060676623.

[17] Vanneste J, Buhler O. Streaming by leaky surface acoustic waves. Proc R Soc A Math Phys Eng Sci 2011;467:1779–800. doi:10.1098/rspa.2010.0457.

[18] Du XY, Fu YQ, Luo JK, Flewitt AJ, Milne WI. Microfluidic pumps employing surface acoustic waves generated in ZnO thin films. J Appl Phys 2009;105:024508. doi:10.1063/1.3068326.

[19] Guo YJ, Lv HB, Li YF, He XL, Zhou J, Luo JK, et al. High frequency microfluidic performance of LiNbO3 and ZnO surface acoustic wave devices. J Appl Phys 2014;116. doi:10.1063/1.4885038.

[20] Liang W, Lindner G. Investigations of droplet movement excited by Lamb waves on a non-piezoelectric substrate. J Appl Phys 2013;114. doi:10.1063/1.4813080.

[21] Luo JT, Geraldi NR, Guan JH, McHale G, Wells GG, Fu YQ. Slippery Liquid-Infused Porous Surfaces and Droplet Transportation by Surface Acoustic Waves. Phys Rev Appl 2017;7:1–9. doi:10.1103/PhysRevApplied.7.014017.

[22] Luo JK, Fu YQ, Li Y, Du XY, Flewitt AJ, Walton AJ, et al. Moving-part-free microfluidic systems for lab-on-a-chip. J Micromechanics Microengineering 2009;19:054001. doi:10.1088/0960-1317/19/5/054001.

[23] Wixforth A. Acoustically driven planar microfluidics. Superlattices Microstruct 2003;33:389–96. doi:10.1016/j.spmi.2004.02.015.

[24] Lee D, Lee N, Choi G, Cho H. Heat Transfer Characteristics of a Focused Surface Acoustic Wave (F-SAW) Device for Interfacial Droplet Jetting. Inventions 2018;3:38. doi:10.3390/inventions3020038.

[25] Darmawan M, Byun D. Focused surface acoustic wave induced jet formation on superhydrophobic surfaces. Microfluid Nanofluidics 2015;18:1107–14. doi:10.1007/s10404-014-1503-y.

[26] Fu C, Quan AJ, Luo JT, Pang HF, Guo YJ, Wu Q, et al. Vertical jetting induced by shear horizontal leaky surface acoustic wave on 36° Y-X LiTaO3. Appl Phys Lett 2017;110:1–6. doi:10.1063/1.4982073.

[27] Fu C, Quan AJ, Luo JT, Pang HF, Guo YJ, Wu Q, et al. Vertical jetting induced by shear horizontal leaky surface acoustic wave on 36° Y-X $LiTaO_3$. Appl Phys Lett 2017;110:173501. doi:10.1063/1.4982073.

[28] Gerold B, Glynne-Jones P, McDougall C, McGloin D, Cochran S, Melzer A, et al. Directed jetting from collapsing cavities exposed to focused ultrasound. Appl Phys Lett 2012;100:2–5. doi:10.1063/1.3676414.

[29] Du XY, Swanwick ME, Fu YQ, Luo JK, Flewitt AJ, Lee DS, et al. Surface acoustic wave induced streaming and pumping in 128° Y-cut $LiNbO_3$ for microfluidic applications. J Micromechanics

Microengineering 2009;19:035016. doi:10.1088/0960-1317/19/3/035016.

[30] Collignon S, Friend J, Yeo L. From chip-in-a-lab to lab-on-a-chip: towards a single handheld electronic system for multiple application-specific lab-on-a-chip (ASLOC) 2014;15. doi:10.1039/c4lc01453g.

[31] Zhang A, Zha Y, Zhang J. A surface acoustic wave micropump to pump fluids from a droplet into a closed microchannel using evaporation and capillary effects. Cit AIP Adv 2014;4. doi:10.1063/1.4905062.

[32] Ai Y, Marrone BL. Droplet translocation by focused surface acoustic waves. Microfluid Nanofluidics 2012;13:715–22. doi:10.1007/s10404-012-0990-y.

[33] Rezk AR, Yeo LY, Friend JR. Poloidal Flow and Toroidal Particle Ring Formation in a Sessile Drop Driven by Megahertz Order Vibration. Langmuir 2014;30:11243–7. doi:10.1021/la502301f.

[34] Riaud A, Baudoin M, Bou Matar O, Thomas J-L, Brunet P. On the influence of viscosity and caustics on acoustic streaming in sessile droplets: an experimental and a numerical study with a cost-effective method. J Fluid Mech 2017;821:384–420. doi:10.1017/jfm.2017.178.

[35] Hirt CW, Nichols BD. Volume of Fluid (VOF) Method for the Dynamics of Free Boundaries*. J Comput Phys 1981;39:201–25.

[36] Dianat M, Skarysz M, Garmory A. A Coupled Level Set and Volume of Fluid method for automotive exterior water management applications. Int J Multiph Flow 2017;91:19–38. doi:10.1016/j.ijmultiphaseflow.2017.01.008.

[37] Sussman M, Puckett EG. A Coupled Level Set and Volume-of-Fluid Method for Computing 3D and Axisymmetric Incompressible Two-Phase Flows. J Comput Phys 2000;162:301–37. doi:10.1006/jcph.2000.6537.

[38] Shen C, Zhang C, Gao M, Li X, Liu Y, Ren L, et al. Investigation of effects of receding contact angle and energy conversion on numerical prediction of receding of the droplet impact onto hydrophilic and superhydrophilic surfaces. Int J Heat Fluid Flow 2018;74:89–109. doi:10.1016/j.ijheatfluidflow.2018.09.015.

[39] Familie M. Numerical Modeling and Investigation of Boiling Phenomena. Thesis 2011:137.

[40] Cox RG. The dynamics of the spreading of liquids on a solid surface. Part 1. Viscous flow. J Fluid Mech 1986;168:169–94. doi:10.1017/S0022112086000332.

[41] Afkhami S, Zaleski S, Bussmann M. A mesh-dependent model for applying dynamic contact angles to VOF simulations. J Comput Phys 2009;228:5370–89. doi:10.1016/J.JCP.2009.04.027.

[42] Fu YQQ, Luo JKK, Du XYY, Flewitt AJJ, Li Y, Markx GHH, et al. Recent developments on ZnO films for acoustic wave based bio-sensing and microfluidic applications: a review. Sensors Actuators, B Chem 2010;143:606–19. doi:10.1016/j.snb.2009.10.010.

[43] Fu YQ, Luo JK, Nguyen NT, Walton AJ, Flewitt AJ, Zu XT, et al. Advances in piezoelectric thin films for acoustic biosensors, acoustofluidics and lab-on-chip applications. Prog Mater Sci 2017;89:31–91. doi:10.1016/j.pmatsci.2017.04.006.

[44] Sankaranarayanan SK, Bhethanabotla VR. Numerical analysis of wave generation and propagation in a focused surface acoustic wave device for potential microfluidics applications. IEEE Trans Ultrason Ferroelectr Freq Control 2009;56:631–43. doi:10.1109/TUFFC.2009.1079.

[45] Jangi M, Luo JT, Tao R, Reboud J, Wilson R, Cooper JM, et al. Concentrated vertical jetting mechanism for isotropically focused Zno/Si surface acoustic waves. Int J Multiph Flow 2019;114:1–8. doi:10.1016/J.IJMULTIPHASEFLOW.2019.02.002.

[46] Alghane M, Chen BX, Fu YQ, Li Y, Luo JK, Walton AJ. Experimental and numerical investigation of acoustic streaming excited by using a surface acoustic wave device on a 128° YX-$LiNbO_3$ substrate. J Micromechanics Microengineering 2011;21:015005. doi:10.1088/0960-1317/21/1/015005.